J Biol Inorg Chem (2006) 11: 467–475
DOI 10.1007/s00775-006-0100-2

ORIGINAL PAPER

E. Vinck · S. Van Doorslaer · S. Dewilde
G. Mitrikas · A. Schweiger · L. Moens

Analyzing heme proteins using EPR techniques: the heme-pocket structure of ferric mouse neuroglobin

Received: 7 September 2005 / Accepted: 23 February 2006 / Published online: 5 April 2006

Abstract In this work, an electron paramagnetic resonance (EPR) strategy to study the heme-pocket structure of low-spin ferric heme proteins is optimized. Frozen solutions of ferric mouse neuroglobin (mNgb) are analyzed by means of electron spin echo envelope modulation and pulsed electron–nuclear double resonance techniques. The hyperfine and nuclear quadrupole couplings of the directly coordinating heme and histidine nitrogens are derived and are discussed in comparison with known data of other ferric porphyrin compounds. In combination with the hyperfine matrices of the imidazole protons, the ^{14}N EPR parameters reveal structural information on the heme pocket of mNgb that is in agreement with previous X-ray diffraction data on neuroglobins.

Keywords Electron paramagnetic resonance · Electron–nuclear double resonance · Electron spin echo envelope modulation · Globin

Abbreviations CP: Combination peak · CW: Continuous wave · dq: Double quantum · ENDOR: Electron–nuclear double resonance · EPR: Electron paramagnetic resonance · ESEEM: Electron spin echo envelope modulation · Hb: Hemoglobin · HYSCORE: Hyperfine sublevel correlation · LS: Low spin · Mb: Myoglobin · 4-MeIm: 4-Methyl imidazole · mNgb: Mouse neuroglobin · mw: Microwave · Ngb: Neuroglobin · NGB: Human neuroglobin · PPIX: Protoporphyrin IX · rf: Radio frequency · TPP: Tetraphenylporphyrin · Tris: Tris(hydroxymethyl) aminomethane · wt: Wild type

Electronic Supplementary Material Supplementary material is available for this article at http://dx.doi.org/10.1007/s00775-006-0100-2 and is accessible for authorized users.

This paper is dedicated to our coauthor Prof. Arthur Schweiger, who passed away unexpectedly on 4 January 2006.

E. Vinck · S. Van Doorslaer (✉)
Department of Physics, University of Antwerp,
Campus Drie Eiken, Universiteitsplein 1,
2610 Wilrijk, Belgium
E-mail: sabine.vandoorslaer@ua.ac.be
Fax: +32-3-8202470

S. Dewilde · L. Moens
Department of Biochemical Sciences, University of Antwerp,
Antwerp, Belgium

G. Mitrikas · A. Schweiger
Physical Chemistry Laboratory, ETH Hönggerberg, HCI,
8093 Zurich, Switzerland

Introduction

Recently, a new member was added to the globin family. It is referred to as neuroglobin (Ngb), since it is mainly expressed in the neuronal cells of the brain and the retina [1]. The function of Ngb is still unclear [2]. The amino acid sequence of this globin deviates significantly from the sequence of myoglobin (Mb) and hemoglobin (Hb) (less than 25% identity), indicating that Ngb is an ancient protein with its own, specific function. Despite the low identity with Mb and Hb, most of the key residues are preserved, such as the histidines at positions E7 and F8. The proximal histidine, F8His, connects the heme group to the surrounding protein chain via a bond with the iron at the center of the heme group. In mammalian Mb and Hb, the opposing side of the heme group (the distal side) is left accessible for external ligands (such as O_2, H_2O, etc.). The E7-histidine (E7H) resides in the vicinity of the distal binding site and can stabilize the binding of an external ligand. In contrast, the distal histidine of both the ferric and the ferrous forms of Ngb is found to bind to the heme iron [2–7], thereby competing with exogenous ligands [2–7].

This results in a slow in vivo binding of exogenous ligands to ferrous Ngb. Also, the observed k_{off} rates for O_2 and CO are very low, owing to the stronger stabilization of these ligands by E7H [5]. In contrast, globins that lack the E7H residue, e.g., *Aplysia* Mb, are found to have k_{on} rates which are similar to those of mammalian

Mbs, while the observed k_{off} rates are much larger [8]. This indicates that E7H plays a key role in the stabilization of exogenous ligand binding. Furthermore, it was shown previously that human Ngb (NGB) can form a disulfide bridge between the cysteins at positions CD7 and D5, with a consequent change in the binding kinetics (the histidine affinity decreases and the oxygen affinity increases) and the heme-pocket structure [9, 10].

Recent X-ray diffraction studies revealed the 3D structure of the bishistidine coordinated form of mouse Ngb* (mNgb*) and human Ngb* (NGB*) (the asterisk indicates that all cysteines have been mutated to serine or glycine; for details see [11, 12]). However, no information is available about the structure of the disulfide-bridged form.

In a previous work [13], we expanded the procedure introduced by Raitsimring et al. [14], which allows us to determine the orientation of the **g** principal axes and the axial ligand orientation in the molecular frame of low-spin (LS) Fe(III) porphyrins. We showed that this method is more accurate if the proton two-pulse electron spin echo modulation (ESEEM) and/or 1D combination peak (CP) data are combined with simulations of the nitrogen and proton hyperfine sublevel correlation (HYSCORE) spectra. The method was tested on a bisimidazole-ligated porphyrin compound [13], and later was used for the structural analysis of tomato Hb, a plant globin displaying a bishistidine coordination [15]. However, these systems are characterized by a (quasi) parallel alignment of the two imidazole planes. This is in contrast to Ngb, where the available X-ray diffraction and continuous wave (CW) electron paramagnetic resonance (EPR) data indicate that the imidazole planes are no longer parallel [6, 11, 12]. In this work, we show how the aforementioned procedure can be expanded to treat the case of nonparallel ligand planes by using pulsed electron–nuclear double resonance (ENDOR). Ferric mNgb is a suitable test globin for two reasons. First of all, X-ray diffraction data [11, 12] are available to verify the structural information obtained from the EPR analysis. Second, our long-term goal is to unravel the changes occurring in the heme-pocket region of NGB upon disulfide-bridge formation. mNgb cannot form a disulfide bridge, since the cysteine at position CD7 is missing and is therefore an ideal model for the NGB form missing the disulfide bridge. It will be shown that the present analysis is the first and necessary step in the unraveling of the heme-pocket change upon disulfide-bridge formation. Furthermore, the EPR parameters will be discussed in terms of the electronic structure of the iron heme group.

Materials and methods

Sample preparation

The wild-type (wt) Ngb expression plasmids (complementary DNA cloned in pET3a) were transformed into *Escherichia coli* strain BL21(DE3)pLysS. The cells were grown at 298 K in TB medium (1.2% bactotryptone, 2.4% yeast extract, 0.4% glycerol, 72 mM potassium phosphate buffer, pH 7.5) containing 200 μg/ml ampicilin, 30 μg/ml chloramphenicol and 1 mM D-aminolevulinic acid. The culture was induced at $A_{550} = 0.8$ by the addition of isopropyl-1-thio-D-galactopyranoside to a final concentration of 0.4 mM and expression was continued overnight. Cells were harvested and resuspended in a lysis buffer [50 mM tris(hydroxymethyl) aminomethane (Tris) HCl, pH 8.0; 1 mM EDTA; 0.5 mM dithiotreitol]. The cells were then exposed to three freeze–thaw steps and were sonicated until completely lysed. The extract was clarified by low-speed (10 min at 10,000*g*) and high-speed (60 min at 105,000*g*) centrifugation and was fractionated by ammonium sulfate precipitation. The 50% ammonium sulfate pellet, containing the crude Ngb, was dissolved in 50 mM Tris–HCl, pH 8.5, dialyzed and loaded onto a (diethylamino)ethyl–Sepharose Fast Flow column equilibrated in the same buffer. After washing of the unbound material, the Ngb was eluted with 200 mM NaCl. The Ngb fractions were concentrated by Amicon filtration (PM10) and passed through a Sephacryl S 200 column. The Ngb fractions were pooled, concentrated and stored at 250 K.

For the EPR measurements, 20% of glycerol was added to the samples as a cryoprotectant. The concentration of the sample was 0.8 mM.

Spectroscopy

The X-band pulsed EPR experiments were performed with an ESP380E Bruker spectrometer [microwave (mw) frequency 9.76 GHz] equipped with a liquid-helium cryostat from Oxford Instruments. All experiments were done at 4 K and a repetition rate of 1 kHz. The magnetic field was measured with a Bruker ER035M NMR gauss meter.

The HYSCORE experiments [16] were carried out using the pulse sequence $\pi/2$-τ-$\pi/2$-t_1-π-t_2-$\pi/2$-τ-echo, with pulse lengths of $t_{\pi/2} = t_{\pi} = 16$ ns. Times t_1 and t_2 were varied from 96 to 5,680 ns in steps of 16 ns. In order to optimize the proton signal intensity, the second and third $\pi/2$ pulses were replaced by matched pulses of 40- or 48-ns length [17].

The 1D and 2D CP experiments [18] were performed with the pulse sequence $\pi/2$-τ-$\pi/2$-T-π-T-$\pi/2$-τ-echo, with pulse lengths of $t_{\pi/2} = t_{\pi} = 16$ ns. The interpulse time T was varied from 96 to 3,288 ns in steps of 8 ns. τ was varied from 96 to 1,688 ns in steps of 8 ns. For both HYSCORE and CP experiments, an eight-step phase cycle was performed to eliminate unwanted echoes. The two-pulse ESEEM experiments were carried out with the following pulse sequence: $\pi/2$-τ-π-τ-echo, with pulse lengths of $t_{\pi/2} = 16$ ns and $t_{\pi} = 32$ ns. τ was varied from 96 to 2,888 ns in steps of 8 ns.

The ENDOR experiments were performed with an Elexsys Bruker spectrometer (mw frequency 9.68 GHz).

All experiments were done at 6 K. The Davies ENDOR experiments [19] were carried out with the pulse sequence π-T-$\pi/2$-τ-π-τ-echo with mw pulse lengths of 200, 100 and 200 ns, respectively, and an interpulse time τ of 550 ns. A radio-frequency (rf) π pulse of variable frequency and a length of 9 μs was applied during time T (10 μs). The Mims ENDOR experiments [20] were performed using the pulse sequence $\pi/2$-τ-$\pi/2$-T-$\pi/2$-τ-echo, with mw pulse lengths of 16 ns and an interpulse time of $\tau = 128$ ns. During time T (10 μs) an rf pulse with variable frequency and a length of 9.5 μs was applied.

Data manipulation

The data were processed with the program MATLAB (MathWorks, Natick, MA, USA). The time traces of the HYSCORE, CP and two-pulse ESEEM experiments were baseline-corrected with a third-order polynomial, apodized with a Hamming window and zero-filled. After 1D or 2D Fourier transformation the absolute-value spectrum was calculated. In order to get a blind-spot-free 1D CP spectrum the τ traces were summed after 1D Fourier transformation.

The HYSCORE spectra were simulated using the programs described in [21, 22]. The same sets of τ values as in the experiments were taken. For the simulation, nonideal pulses were used with the same pulse lengths as in the experiment. The Euler angles α, β and γ define an active rotation (right-hand) of the **g** principal axes system with respect to the matrices and tensors (i.e., rotation about the z-axis over angle α, followed by rotation of angle β about the new y axis, with subsequent rotation about the new z-axis over angle γ). The ENDOR simulations were done with the EasySpin program, a Matlab toolbox developed for EPR simulations [23]. The proton combination frequencies in the 1D CP and the two-pulse ESEEM spectra were analyzed using the procedure outlined in [14].

Theory

The spin Hamiltonian of an Fe(III) LS system is given by

$$H = \beta_e \tilde{B}_0 g S/h + \sum_k \tilde{S} A_k I_k - \beta_n \sum_k g_{n,k} \tilde{B}_0 I_k/h + \sum_{I>1/2} \tilde{I}_k P_k I_k \quad (1)$$

and contains the electron-Zeeman interaction, the hyperfine interactions, the nuclear-Zeeman interactions and the nuclear quadrupole interactions [24]. The electron-Zeeman interaction is characterized by the **g** matrix. Earlier studies revealed that LS ferric heme systems have a rhombic **g** matrix, with principal values $g_z > g_y > g_x$, whereby the g_z principal axis is in most cases normal to the heme plane and g_x and g_y lie in the heme plane [25]. The **g** matrix is related to the coefficients of the d_{xz}, d_{xy} and d_{yz} orbitals of the heme iron. For LS ferric porphyrins, it was found that most of the unpaired electron spin density resides in the highest d_{yz} orbital, with small amounts mixed into the d_{xz} and d_{xy} orbitals owing to the spin–orbit coupling. The nuclear quadrupole interaction only occurs for nuclear spins larger than 1/2, such as ^{14}N with nuclear spin $I = 1$. The nuclear quadrupole principal values are denoted as P_1, P_2 and P_3, with $|P_1| > |P_2| > |P_3|$. An $S = 1/2$, $I = 1$ system is characterized by four single-quantum nuclear transitions ($|\Delta m_S| = 0$, $|\Delta m_I| = 1$) and two double-quantum (dq) nuclear transitions ($|\Delta m_S| = 0$, $|\Delta m_I| = 2$). These dq transitions will produce strong cross-peaks in the HYSCORE spectra. Throughout this article, the frequencies related to these transitions are marked as dq_α and dq_β, for the α and β electron spin manifolds, respectively. In an $S = 1/2$, $I = 1/2$ system only single-quantum transitions exist. ENDOR experiments allow one to measure the nuclear transition frequencies of the spin system, which are related to the hyperfine and nuclear quadrupole tensors of the spin system.

Results and discussion

The nitrogen HYSCORE spectra of ferric wt mNgb recorded at magnetic field positions near g_x, g_y and g_z are depicted in Fig. 1. The spectra are very similar to the HYSCORE spectra of the bisimidazole-ligated porphyrin compounds, iron(III) tetraphenylporphyrin bis(4-methylimidazole) [Fe(III)TPP(4-MeIm)$_2$] and iron(III) protoporphyrin IX bis(imidazole) [Fe(III)PPIX(Im)$_2$] [13, 26]. For these porphyrin compounds, as well as for ferric wt mNgb, two different sets of (dq_α,dq_β) cross-peaks appear in the HYSCORE spectra (Fig. 1). The assignment of these cross-peaks to the different nitrogens is based on the work of García-Rubio et al. [26] (see the supplementary material for details), and is shown in Fig. 1.

Note that only one type of imidazole nitrogen (dq^i_α,dq^i_β) peak can be discerned in the HYSCORE spectra of ferric wt mNgb, indicating that both the proximal and the distal histidines reside at similar distances from the iron atom. Furthermore, from the combination frequencies observed in the HYSCORE spectra it can be derived that the hyperfine interactions of the imidazole and porphyrin nitrogens have the same sign (see supplementary material). This is in agreement with previous density functional theory work on LS iron(III) porphyrins, where it was shown that both the porphyrin and the imidazole hyperfine couplings have a negative sign owing to an excess of β spin density in the nitrogen s orbitals [27].

As we pointed out in our previous work [13], it is not possible to take into account the full seven-spin system in the HYSCORE simulations (i.e., $S = 1/2$, four por-

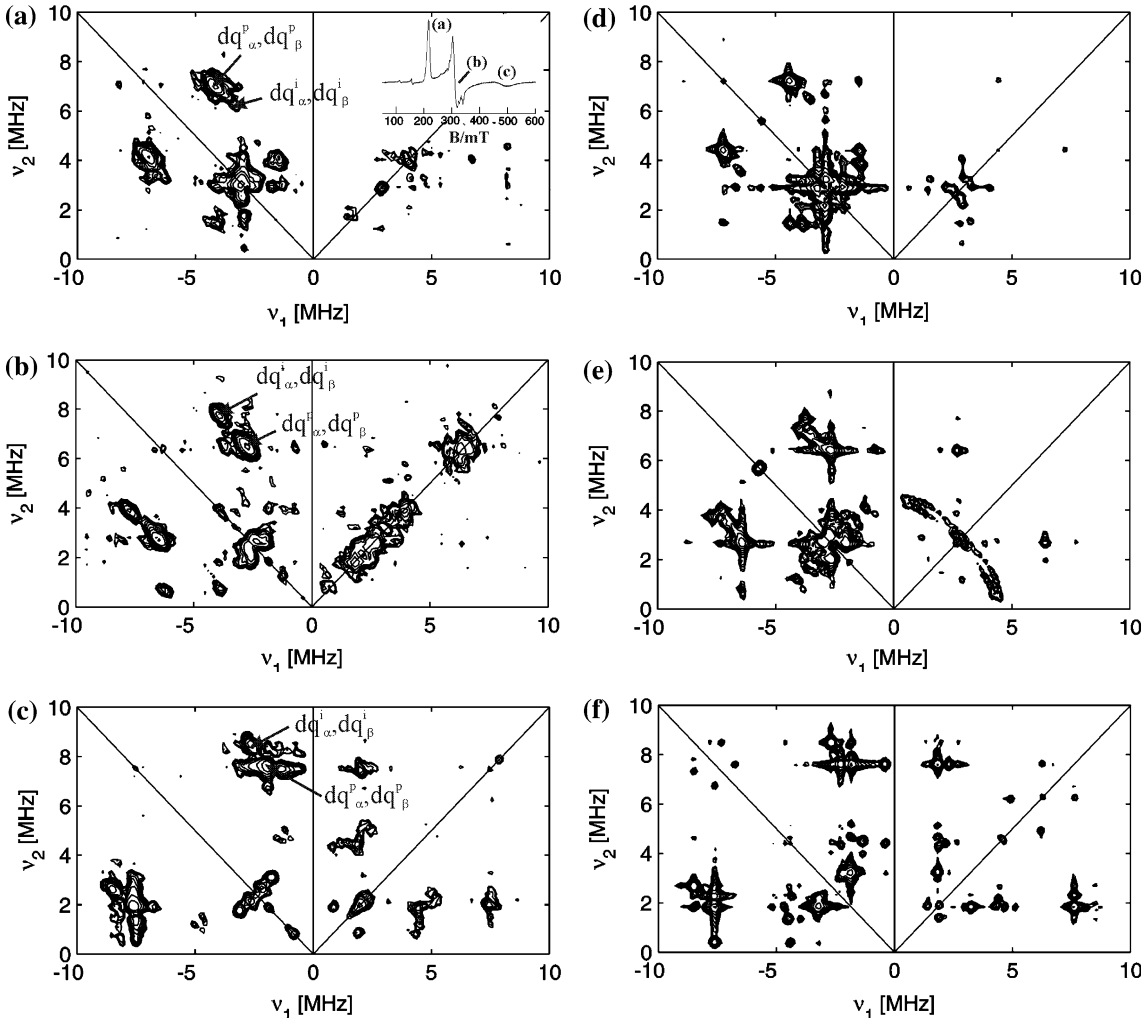

Fig. 1 Experimental (**a**–**c**) and simulated (**d**–**f**) nitrogen hyperfine sublevel correlation (*HYSCORE*) spectra of ferric wild-type mouse neuroglobin (*wt mNgb*) at different magnetic field positions. The *inset* in **a** is the continuous-wave electron paramagnetic resonsnce spectrum of ferric wt mNgb, with the observer positions of the experimental HYSCORE spectra (**a**–**c**). **a**, **d** Observer position $g = 2.79$. **b**, **e** Observer position $g = 2.12$. **c**, **f** Observer position $g = 1.36$. In all experimental spectra the double-quantum (*dq*) cross-peaks of the porphyrin nitrogens ($dq^{p}_{\alpha},dq^{p}_{\beta}$) and imidazole nitrogens ($dq^{i}_{\alpha},dq^{i}_{\beta}$) are indicated. The simulations were done for a four-spin system: $S = 1/2$, N_{p1}, N_{p2}, N_i using the parameters shown in Table 1 (porphyrin nitrogens, $n = 0$, 1, imidazole parameters for im1). [Similar simulations were performed for im2, resulting in equally good agreements with the experiment (not shown)]

phyrin nitrogens and two imidazole nitrogens), as this would lead to unrealistic computation times; therefore, the present simulations were done with a four-spin system: $S = 1/2$, two mutually perpendicular porphyrin nitrogens ($n = 0$, 1 in Table 1) and one imidazole nitrogen. The experimental HYSCORE spectra could be simulated satisfactorily with this limited set of spins (Fig. 1). Other combinations of porphyrin nitrogens were tried ($n = 0$, 2; $n = 1$, 3) but these did not improve the simulations. The simulations were hardly sensitive to variation of the Euler angle α of the imidazole hyperfine and the nuclear quadrupole principal axes (this is the angle between g_x and the imidazole plane), mainly because the single-quantum cross-peaks of the imidazole nitrogens are largely masked by those of the porphyrin nitrogens. Both sets of imidazole principal values in Table 1 (corresponding to im1 and im2) gave equally good results.

The X-band ENDOR spectra at different magnetic field positions are shown in Fig. 2. Several peaks can be discerned. For simulation of the ENDOR spectra, a five-spin system was used [i.e., $S = 1/2$, two porphyrin nitrogens ($n = 0$, 1), and two imidazole nitrogens]. The simulations were done in the following way. First, the hyperfine and nuclear quadrupole values of the porphyrin nitrogens obtained from simulation of the nitrogen HYSCORE spectra were used for the ENDOR simulations, which allowed the assignment of the porphyrin nitrogen ENDOR peaks. Next, the imidazole nitrogen hyperfine and nuclear quadrupole values obtained from the HYSCORE simulations were optimized by simulation of the remaining ENDOR peaks.

Table 1 Hyperfine and nuclear quadrupole parameters of the porphyrin nitrogens (*por*) and the directly coordinated imidazole nitrogens (*im*) of ferric wild-type mouse neuroglobin (*wt mNgb*) and Fe(III)TPP(4-MeIm)$_2$ (*TPP* tetraphenylporphyrin, *4-MeIm* 4-methyl imidazole) [13]

	$\|A_1\|$ (MHz)	$\|A_2\|$ (MHz)	$\|A_3\|$ (MHz)	$\|a_{iso}\|$ (MHz)	P_1 (MHz)	P_2 (MHz)	P_3 (MHz)
FeTPP(4-MeIm)$_2$/por	4.8	4.8	5.8	5.1	−0.42	−0.51	0.93
	$\alpha, \beta, \gamma = 0 \pm 15°, 0 \pm 20°, n90 \pm 25°$				$\alpha, \beta, \gamma = 0 \pm 15°, 90 \pm 20°, n90 \pm 25°$		
Ferric wt mNgb/por	4.2	4.2	5.7	4.7	−0.43	−0.52	0.95
	$\alpha, \beta, \gamma = 0 \pm 5°, 0 \pm 20°, (n90 + 10) \pm 10°$				$\alpha, \beta, \gamma = 90 \pm 5°, 90 \pm 20°, (n90 + 10) \pm 10°$		
FeTPP(4-MeIm)$_2$/im	5.7	6.2	5.3	5.7	0.34	0.51	−0.85
	$\alpha, \beta, \gamma = 0 \pm 15°, 0 \pm 15°, 0 \pm 15°$				$\alpha, \beta, \gamma = 0 \pm 15°, 0 \pm 15°, 0 \pm 15°$		
Ferric wt mNgb/im1	5.25	5.65	4.9	5.3	0.16	0.64	−0.8
	$\alpha, \beta, \gamma = 10 \pm 25°, 0 \pm 25°, 0 \pm 25°$				$\alpha, \beta, \gamma = 10 \pm 25°, 0 \pm 25°, 0 \pm 25°$		
Ferric wt mNgb/im2	5.25	5.65	4.9	5.3	0.3	0.55	−0.85
	$\alpha, \beta, \gamma = 50 \pm 25°, 0 \pm 25°, 0 \pm 25°$				$\alpha, \beta, \gamma = 50 \pm 25°, 0 \pm 25°, 0 \pm 25°$		

The orientations of the imidazole and porphyrin nitrogen hyperfine and nuclear quadrupole tensors are shown in Fig. 3. $n = 0, 1, 2, 3$. Experimental errors are 0.3 MHz for $|A_1|$, $|A_2|$ and $|A_3|$; 0.15 MHz for P_1 and P_2; 0.1 MHz for P_3

The nitrogen HYSCORE (and ENDOR) simulations allow us to determine the orientation of the **g** principal axes in the molecular frame, as outlined in previous publications [13, 15]. For a detailed description of this analysis in the mNgb case, we refer to the supplementary material. The g_z axis of ferric mNgb was found to be parallel to the heme normal (within 15°), whereas the in-plane **g** axes (g_x and g_y) almost coincide with the Fe–N_p axes ($10 \pm 10°$).

This information can now be used to derive the orientation of the imidazole planes in the molecular frame. Unfortunately, the nitrogen HYSCORE and ENDOR simulations were not very sensitive to variation of the Euler angle α of the imidazole hyperfine and nuclear quadrupole values (i.e., the angle between the g_x axis and the imidazole plane) owing to the partial overlap of the imidazole and porphyrin nitrogen contributions. Simulation of the nitrogen ENDOR spectra allowed only for a very rough estimation of the orientation of the two imidazole planes in the heme pocket (Fig. 3). The Euler angles listed in Table 1 were obtained after simulation of the proton ESEEM and ENDOR spectra.

A first estimation of the proton hyperfine parameters can be obtained from simulation of the two-pulse ESEEM and 1D CP spectra. For a detailed description of this procedure, we refer to earlier work [13, 14] and the supplementary material. In this section, we repeat only the most important points. The proton 1D CP and two-pulse ESEEM spectra (Fig. 4) consist of two peaks: (1) a peak at twice the proton Larmor frequency due to

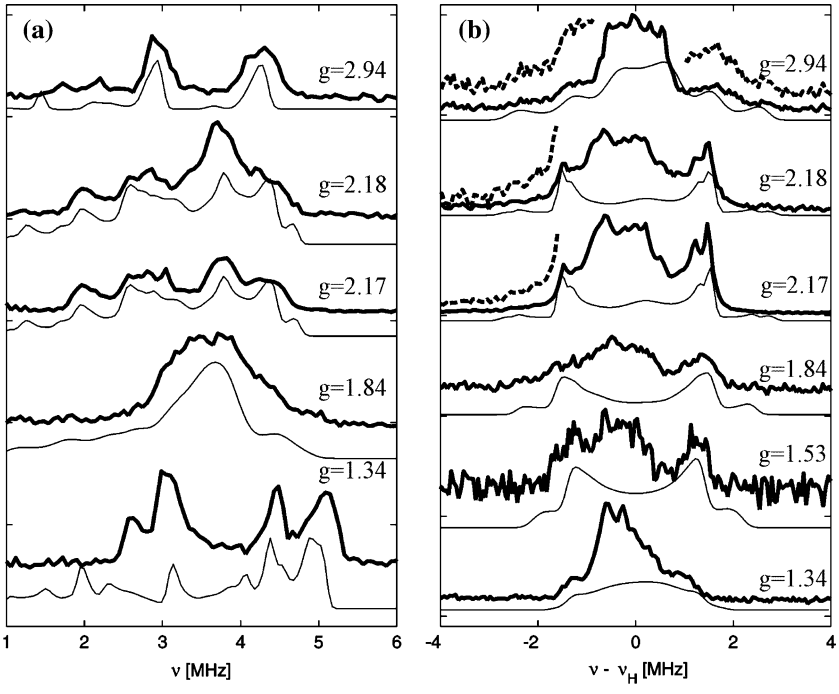

Fig. 2 Experimental (*thick lines*) and simulated (*thin lines*) electron–nuclear double resonance (*ENDOR*) spectra. **a** Nitrogen ENDOR spectra, **b** proton ENDOR spectra. The *dashed lines* in **b** are the threefold magnifications of the underlying region of the experimental spectrum. The simulations in **a** were done for a five-spin system: $S = 1/2$, N_{p1}, N_{p2}, N_{i1}, N_{i2}, using the parameters shown in Table 1, with $n = 0, 1$. For the simulations in **b**, a three-spin system was used: $S = 1/2$, H_1 and H_2 (for the simulation parameters, see the text). The ENDOR spectra at magnetic field positions in the range from $g = 2.94$ to $g = 1.53$ were recorded with a Davies ENDOR pulse sequence, whereas the spectrum at $g = 1.34$ was recorded with a Mims ENDOR pulse sequence

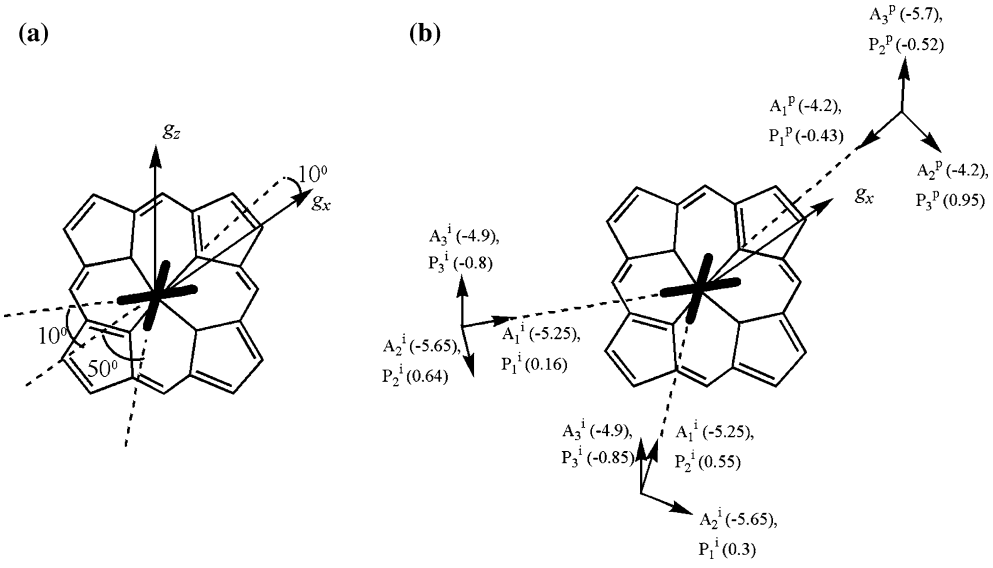

Fig. 3 The heme-pocket structure of ferric wt mNgb. **a** Optimal solution of the orientation of the **g** matrix and the imidazole planes in agreement with both the simulations and the counter-rotation principle (see further). **b** Orientation of the nuclear quadrupole and hyperfine tensors of the imidazole and porphyrin nitrogens. The principal values in *parentheses* are given in megahertz. The parameters shown in **b** correspond to those in Table 1, with $n = 1$

the many distant protons of the protein and (2) a peak which is shifted to higher frequencies representing the nearest protons of the imidazole ring (these are the protons of the histidine imidazole that reside closest to the heme iron). The magnetic field dependence of the shift of the nearest-proton peak from twice the proton Larmor frequency can be related to the distance R between the iron atom and the corresponding proton, the isotropic hyperfine coupling constant a_{iso} and the orientation of the iron-nearest proton (Fe–H) axis [14]. The latter is defined by the angle θ between the g_z axis and the Fe–H bond and the angle φ between the projection of the Fe–H axis in the (g_x, g_y) plane and the g_x axis. The simulated two-pulse and 1D CP spectra are shown in Fig. 4. In the two-pulse ESEEM spectra, the contribution from the distant protons was approximated by taking into account 50 protons at a distance of 0.7 nm (Fig. 4a). For the 1D CP experiments, only the nearest-proton peak of the spectra was simulated (Fig. 4b). Note that in the 1D CP spectrum at the highest magnetic field position (lowest g) the simulated nearest-proton peak deviates from the experimental one. Possibly, this shift is induced by the overlap with the distant-proton peak. From these simulations (Fig. 4), the distance R was estimated to be 0.325 ± 0.01 nm. The angle θ lies in the range 35–45°. The spectra were not very sensitive to variations of the angle φ and a_{iso}, which is due to the fact that the nearest-proton peak could only be resolved at the lowest magnetic field settings.

Our earlier analysis of synthetic Fe(III) complexes showed that the CP experiments need to be complemented by proton HYSCORE experiments in order to obtain the full set of proton hyperfine parameters with high accuracy [13]. However, owing to the high magnetic field setting and the large g-strain effects in the present case, no proton HYSCORE could be obtained at

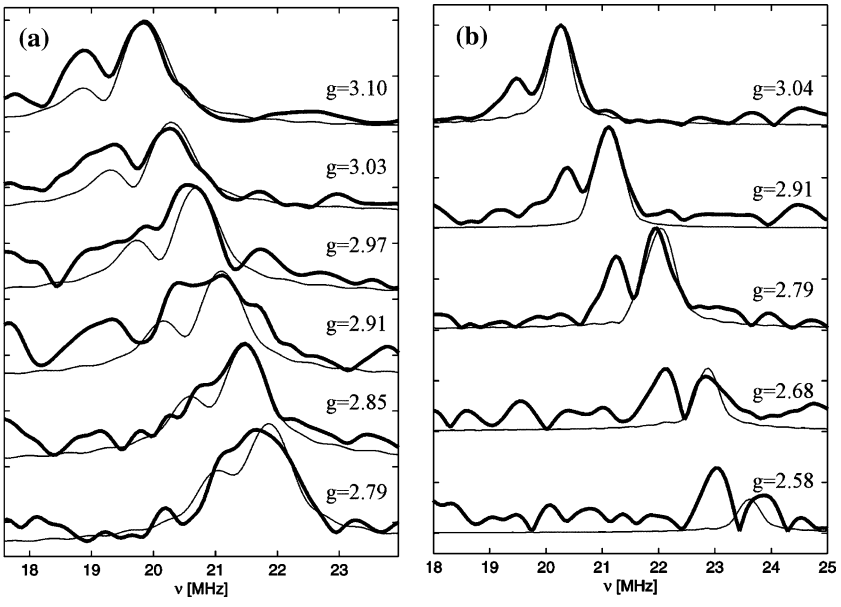

Fig. 4 A selection of experimental (*thick lines*) two-pulse proton electron spin echo envelope modulation spectra (**a**) and proton 1D combination peak spectra (**b**), and simulations (*thin lines*). The simulation parameters are $R = 0.325$ nm, $\theta = 40°$

observer positions near $g = g_x$. At these observer positions, Mims ENDOR spectra could still be recorded. Furthermore, the broad ridge form of the proton HYSCORE signal and the τ-dependent blind-spot effect makes it difficult to distinguish overlapping contributions of protons with slightly differing hyperfine parameters. From the proton HYSCORE simulations, a first estimation of the proton hyperfine values could be derived (see supplementary material). The HYSCORE spectra at the magnetic field position corresponding to $g = g_z$ are most sensitive to variation of the Euler angle β of the hyperfine tensor. The best correspondence between experimental and simulated spectra is obtained for β values between 30 and 55°.

The experimental and simulated proton ENDOR spectra are shown in Fig. 2b. Contributions from a large number of protons can be discerned in the proton ENDOR spectra. This contrasts with the case for the proton 1D CP spectra, where only a distant-proton-type and a nearest-proton-type peak can be resolved. As no isotopic substitution of the protons was done, it is impossible to assign the different peaks to specific protons. However, in agreement with the 1D CP and two-pulse ESEEM spectra, we can assign the ENDOR peaks with the largest splittings to the nearest protons of the imidazole ring. This is justified by previous CW ENDOR studies on bisimidazole-ligated porphyrin compounds [28], where it was found—by isotopic substitution—that the porphyrin protons are more weakly coupled than the imidazole protons (porphyrin proton couplings lie in the range 0.5–2 MHz). All the spectra were recorded using the Davies ENDOR technique with the exception of the spectrum at a magnetic field position corresponding to $g = 1.34$ (Mims ENDOR). This was done because the intensity of the spin echo signal was very low at this magnetic field position and even Mims ENDOR experiments required integration times of approximately 24 h. All ENDOR spectra show significant asymmetry in the line intensities, although the effect is most prominent for the Mims ENDOR spectrum. The latter may be due to the implicit TRIPLE effect known to occur in Mims ENDOR spectra of $S = 1/2$ systems coupled to both ^{1}H and ^{14}N nuclei [29]. However, this is not a valid interpretation for the asymmetry occurring in the Davis ENDOR spectra. The origin of the intensity asymmetry is unclear, since the nuclear transition saturation effects shown to modulate Davies ENDOR intensities at the W-band [30] are very unlikely at the X-band owing to the low thermal polarization.

In order to simulate all the contributions from strongly coupled protons in the ENDOR spectra, at least two different types of protons have to be taken into account. The optimized proton hyperfine values that agree with both the ENDOR and the HYSCORE simulations are (1) $(A_1\ A_2\ A_3) = (-2.7 \pm 0.5, -2.7 \pm 0.5, 6.0 \pm 0.5)$ MHz, $(\alpha_A\ \beta_A\ \gamma_A) = (0 \pm 10°,\ 38 \pm 5°,\ 50 \pm 20°)$, and (2) $(A_1\ A_2\ A_3) = (-3.1 \pm 0.5,\ -3.1 \pm 0.5,\ 5.0 \pm 0.5)$ MHz, $(\alpha_A\ \beta_A\ \gamma_A) = (0 \pm 10°, 45 \pm 5°, -10 \pm 20°)$.

The absolute sign of the proton hyperfine parameters was taken in accordance with earlier studies on similar systems [14].

For protons, the dipolar part of the hyperfine interaction can be approximated using the point-dipole model under the condition that the distances between the unpaired electron and the protons are relatively large (more than 0.25 nm) [31]. The hyperfine matrix is then

$$\mathbf{A} = a_{\mathrm{iso}} + (\mathbf{g}/g_e)\mathbf{T}, \tag{2}$$

with

$$\mathbf{T} = \left(\frac{\mu_0}{4\pi h}\right)(g_n\beta_e\beta_n g_e)(3\mathbf{n}\mathbf{n}^{\dagger} - \mathbf{1})/R^3, \tag{3}$$

where R is the Fe–H distance and $\mathbf{n}$ is the vector between the proton and the Fe nucleus. The hyperfine principal values mentioned before agree best with (1) $R = 0.325 \pm 0.010$ nm and $a_{\mathrm{iso}} = -0.4 \pm 0.5$ MHz and (2) $R = 0.335 \pm 0.010$ nm and $a_{\mathrm{iso}} = -1.3 \pm 0.5$ MHz. These values of R compare well with those found by simulation of the 1D CP and two-pulse ESEEM spectra ($R \sim 0.325$ nm). Note that it was impossible to exactly reproduce the experimental hyperfine matrices using Eq. 2. This is due to the simplicity of the point-dipole model and the experimental errors. The value of a_{iso} is in agreement with values from previous NMR studies on LS ferric porphyrin compounds [32].

The simulated angles between the g_x axis and the imidazole planes at the distal and proximal sides of the heme group amount to $50 \pm 20°$ and $10 \pm 20°$, whereas the angle between the g_x axis and the Fe–N_p bond amounts to $10 \pm 10°$. This means that there still exist a large number of possible solutions. As pointed out in previous publications [13, 15], the number of possible solutions can be reduced significantly by using the principle of counter rotation [33]. This principle states that if the g_x axis deviates over an angle ζ from the Fe–N_p axis, the (parallel) ligand planes will rotate over an angle ζ_0 in the counter direction. A simple one-electron treatment gives $\zeta = -\zeta_0$, whereas more thorough theoretical derivations show that this is too strict a rule. However, one can use the following rule of thumb: if $-45° < \zeta < 0°$, ζ will not exceed 45°. Note that the principle was derived for parallel imidazole planes. In [33] it is suggested that, for the case of a perpendicular alignment of the imidazole planes, the average imidazole plane obeys the principle of counter rotation. Application of this rule to the present results gives an optimal solution for $\zeta = 10 \pm 10°$ and $\zeta_0 = 10 \pm 10°$ (for the average ligand plane orientation) (Fig. 3).

As we mentioned in the "Introduction" X-ray diffraction studies of NGB* and mNgb* were presented previously (the asterisk indicates that all cysteines have been mutated to serine or glycine; for details see [11, 12]). In both proteins, no disulfide bridge is present. In Table 2, the heme-pocket structure of these Ngbs is compared with our results. The orientation of the imidazole planes in the molecular frame of NGB* and

Table 2 The heme-pocket structure of ferric wt mNgb obtained from the present pulsed electron paramagnetic resonance experiments compared with the heme-pocket structure of human Ngb and mNgb where cysteines have been mutated to serine or glycine (*NGB** and *mNgb**), as obtained by X-ray diffraction experiments

	$\chi_{0,d}$ (degrees)	$\chi_{0,p}$ (degrees)	$\Delta\varphi$ (degrees)	ε_d (degrees)	ε_p (degrees)	R_d (nm)	R_p (nm)	Reference
NGB*[a]	34	30	64	39, 41	37, 44	0.335, 0.330	0.339, 0.315	[12]
mNgb*[b]	37	21	58	39, 44	38, 42	0.331, 0.307	0.344, 0.325	[11]
Ferric wt mNgb	40 ± 20, 20 ± 20		60 ± 20	38 ± 5, 45 ± 5		0.325 ± 0.010, 0.335 ± 0.010		This work

In the mNgb* case the structure parameters are derived from the data as deposited in the RCSB Protein Data Bank. The structure parameters compared are as follows. (1) $\chi_{0,d}$ ($\chi_{0,p}$): the angle between the distal (proximal) imidazole plane and the iron–porphyrin nitrogen (Fe–N_p) bond. (2) $\Delta\varphi$: the angle between the distal and proximal imidazole plane. (3) ε_d (ε_p): for NGB* and mNgb* this is the angle between the distal (proximal) iron-imidazole nearest-proton direction and the distal (proximal) iron-imidazole imino nitrogen bond. Two values are given, for each of the two imidazole protons. For ferric wt mNgb, this is the Euler angle β of the nearest-proton hyperfine tensor. (4) R_p and R_d: the distance between the heme iron and the proximal and distal imidazole nearest proton

[a]Values are shown as averages for the four different subunits of the NGB* crystal

[b]Values are given for the most abundant heme-pocket structure (70%)

mNgb* is in good agreement with the pulse EPR results. In all cases ζ of the average ligand plane was found to be close to 0° ($\pm 10°$), and a mutual angle between the proximal and distal imidazole planes of approximately 60° was found. The X-ray data of mNgb* revealed the presence of two conformers, whereby the heme is inserted differently in the protein [11]. These two conformers were not as such found in the X-ray structure of NGB*, although the four molecules present in the crystallographic asymmetric unit showed slight differences in the heme-pocket structure [12]. Since the pulsed EPR measurements were performed on frozen solutions and not on single crystals, the accuracy does not allow for a clear distinction between the two conformers observed in mNgb*.

In our earlier work, we showed that the g values of wt mNgb ($g_x = 1.29 \pm 0.05$, $g_y = 2.15 \pm 0.02$ and $g_z = 3.12 \pm 0.02$ [6, 10]) indicate that the imidazole planes are no longer parallel, but also not yet fully perpendicular, and that the base planes do not eclipse the Fe–N_p bonds, in agreement with our present results.

From Table 1 it is clear that the average hyperfine values $(A_1 + A_2 + A_3)/3$ of the imidazole and porphyrin nitrogens are smaller (in absolute values) for ferric wt mNgb (−5.3 and −4.7 MHz, respectively) than for Fe(III)TPP(4-MeIm)$_2$ (−5.7 and −5.1 MHz, respectively), indicating a decrease in β spin density. For ferric tomato Hb, this trend was similar for the porphyrin nitrogens, but was less pronounced for the imidazole nitrogens [15]. This indicates that the former effect is governed by the change of the porphyrin type (heme vs. TPP), and that the latter reduction is due to the change in the histidine-ligand orientation. Note that the average hyperfine value is not exactly equal to the Fermi contact interaction, because the dipolar-interaction matrix will no longer be traceless owing to the large **g** anisotropy.

This analysis of the electronic and geometric structure of ferric wt mNgb shows that pulsed EPR techniques provide a powerful tool to unravel the heme-pocket structure of Ngb. The structural data obtained from the EPR analysis agree well with the available X-ray data. EPR techniques can therefore be used confidently to study the heme-pocket structure of NGB. Earlier work showed that NGB can form a disulfide bridge that induces changes in the ligand-binding kinetics and therefore in the heme-pocket structure [9, 10]. No information is available about the heme-pocket structure of the disulfide-bridged protein, since crystallization of this protein form failed. Under oxidizing conditions, the EPR spectrum of ferric NGB consists of overlapping contributions from both the species with and without the disulfide bridge [10]. The EPR work on mNgb presented here—an Ngb that cannot form this disulfide bridge—can be used as a blueprint for ferric NGB without a disulfide bridge. The study will facilitate distinction between the different spectral contributions in the pulsed EPR data of ferric NGB, which is necessary to determine the structure of the sulfur-bridged form. These analyses are currently being performed.

Conclusion

In this work we presented a pulsed EPR analysis of the heme-pocket structure of ferric mNgb in which the electronic structure is linked to the geometric findings. It was outlined how the procedure derived earlier to study LS Fe(III) porphyrin systems needs to be complemented with ENDOR analyses in the case of ferric globins characterized by a large **g** anisotropy. The agreements with the available X-ray structures give confidence in the analysis and show that these techniques can be used to investigate unknown forms of Ngb.

Acknowledgment This work was supported by the Fund for Scientific Research-Flanders (FWO) Grant G.0468.03 (to S.V.D) and Grant QLRT-2001-01548 from the European Union. S.D. is a postdoctoral fellow of the FWO. E.V. is a research assistant of the FWO. S.V.D. wants to thank Martino Bolognesi (Universities of Milano and Genova) for interesting discussions on the X-ray data of Ngb proteins.

References

1. Burmester T, Weich B, Reinhardt S, Hankeln T (2000) Nature 407:520–523
2. Pesce A, Bolognesi M, Bocedi A, Ascenzi P, Dewilde S, Moens L, Hankeln T, Burmester T (2002) EMBO Rep 3:1146–1151
3. Couture M, Burmester T, Hankeln T, Rousseau D (2001) J Biol Chem 276:36377–36382
4. Trent JT, Watts RA, Hargrove MS (2001) J Biol Chem 276:30106–30110
5. Dewilde S, Kiger L, Burmester T, Hankeln T, Baudin-Creuza V, Aerts T, Marden MC, Caubergs R, Moens L (2001) J Biol Chem 276:38949–38955
6. Nistor SV, Goovaerts E, Van Doorslaer S, Dewilde S, Moens L (2002) Chem Phys Lett 361:355–361
7. Van Doorslaer S, Dewilde S, Kiger L, Nistor SV, Goovaerts E, Marden MC, Moens L (2003) J Biol Chem 278:4919–4925
8. Shikama K, Matsuoka A (2004) Crit Rev Biochem Mol 39:217–259
9. Hamdane D, Kiger L, Dewilde S, Green BN, Pesce A, Uzan J, Burmester T, Hankeln T, Bolognesi M, Moens L, Marden MC (2003) J Biol Chem 278:51713–51721
10. Vinck E, Van Doorslaer S, Dewilde S, Moens L (2004) J Am Chem Soc 126:4516–4517
11. Vallone B, Nienhaus K, Brunori M, Nienhaus GU (2004) Proteins 56:85–92
12. Pesce A, Dewilde S, Nardini M, Moens L, Ascenzi P, Hankeln T, Burmester T, Bolognesi M (2003) Structure 11:1087–1095
13. Vinck E, Van Doorslaer S (2004) Phys Chem Chem Phys 6:5324–5330
14. Raitsimring AM, Borbat P, Shokhireva TK, Walker FA (1996) J Phys Chem 100:5235–5244
15. Ioanitescu I, Dewilde S, Kiger L, Marden MC, Moens L, Van Doorslaer S (2005) Biophys J 89:2628–2639
16. Höfer P, Grupp A, Nebenführ H, Mehring M (1986) Chem Phys Lett 132:279–282
17. Jeschke G, Rakhmatullin R, Schweiger A (1998) J Magn Reson 131:261–271
18. Van Doorslaer S, Schweiger A (1997) Chem Phys Lett 281:297–305
19. Davies ER (1974) Phys Lett A 47:1–2
20. Mims WB (1965) Proc R Soc Lond 283:452–457
21. Smith SA, Levante TO, Meier BH, Ernst RR (1994) J Magn Reson A 106:75–105
22. Madi Z, Van Doorslaer S, Schweiger A (2002) J Magn Reson 154:181–191
23. Stoll S, Schweiger A (2005) J Magn Reson 177:390–403
24. Schweiger A, Jeschke G (2001) Principles of pulse electron paramagnetic resonance. Oxford University Press, Oxford
25. Hori H (1971) Biochim Biophys Acta 251:227–235
26. García-Rubio I, Martínez JI, Picorel R, Yruela I, Alonso PJ (2003) J Am Chem Soc 125:15846–15854
27. Johansson MP, Sundholm D, Gerfen G, Wilkström M (2002) J Am Chem Soc 124:11771–11780
28. Scholes CP, Falkowski KM, Chen S, Bank J (1986) J Am Chem Soc 108:1660–1671
29. Doan PE, Nelson MJ, Jin H, Hoffman BM (1996) J Am Chem Soc 118:7014–7015
30. Epel B, Pöppl A, Manikandan P, Vega, Goldfarb D (2001) J Magn Reson 148:388–397
31. Hurst GC, Henderson TA, Kreilick RW (1985) J Am Chem Soc 107:7294–7299
32. Satterlee JD, La Mar GN (1976) J Am Chem Soc 98:2804–2808
33. Shokhirev NV, Walker FA (1998) J Am Chem Soc 120:981–990